applied sciences

MDPI

Article

Influence of Oxygen Impurity on Nitrogen Atmospheric-Pressure Plasma Jet

Jia-Shiuan Tsai [1] and Jian-Zhang Chen [1,2,3,4,*]

[1] Graduate Institute of Applied Mechanics, National Taiwan University, Taipei City 106319, Taiwan
[2] Graduate School of Advanced Technology, National Taiwan University, Taipei City 106319, Taiwan
[3] Advanced Research Center for Green Materials Science and Technology, National Taiwan University, Taipei City 106319, Taiwan
[4] Innovative Photonics Advanced Research Center (i-PARC), National Taiwan University, Taipei City 106319, Taiwan
* Correspondence: jchen@ntu.edu.tw; Tel.: +886-2-3366-5694

Abstract: This study discussed the effect of oxygen impurity in the inlet gas of a nitrogen atmospheric pressure plasma jet (APPJ). A numerical model that takes into account the fluid dynamics, heat transfer, mass transfer, diffusion, and chemical reactions was developed to simulate the nitrogen APPJ. Further, a DC nitrogen APPJ experiment was performed to verify the plasma temperature characteristics on the treated surface. The plasma temperature decreased with an increase in the oxygen impurity. Moreover, the oxygen impurity influenced the related excited and neutral species. Specifically, with added oxygen impurity, N-related species decreased whereas O- and NO_x-related species increased. Because the excited state species constitutes the most important reactant in APPJ treatment, this study could serve as a reference for the adjustment of a nitrogen APPJ.

Keywords: atmospheric pressure plasma jet (APPJ); atmospheric pressure plasma; nitrogen plasma; simulation; impurity

check for updates

Citation: Tsai, J.-S.; Chen, J.-Z. Influence of Oxygen Impurity on Nitrogen Atmospheric-Pressure Plasma Jet. *Appl. Sci.* **2023**, *13*, 4199. https://doi.org/10.3390/app13074199

Academic Editor: Emilio Martines

Received: 6 March 2023
Revised: 22 March 2023
Accepted: 24 March 2023
Published: 26 March 2023

Copyright: © 2023 by the authors. Licensee MDPI, Basel, Switzerland. This article is an open access article distributed under the terms and conditions of the Creative Commons Attribution (CC BY) license (https://creativecommons.org/licenses/by/4.0/).

1. Introduction

Atmospheric pressure plasma jets (APPJs) are inexpensive to produce because they do not require vacuum equipment [1–3]. Therefore, they are considered promising for plasma treatment applications in material surface treatment [4–7] and biomedicine [8–11]. The DC pulse nitrogen APPJ with a quartz tube discussed in this paper was proved to improve the power conversion efficiency of Perovskite solar cells better and within a shorter treatment time compared with DBD plasma and UV ozone treatment [6]. However, the amount of excited species on the treated surface cannot easily be evaluated through experiments because of the limitations of measuring techniques.

Studies have simulated [12,13] APPJ propagation in a transient state and used models to calculate the electronic and magnetic properties and chemical reactions. As a result, streamer and electric field propagation characteristics have been obtained. To improve mass transfer in the fluid flow downstream, combinations of laminar [14], large-eddy simulation (LES) [15], and k-ε and k-ω turbulent models [16,17] in commercial computational fluid dynamics (CFD) software or user-defined code [18–20] have been used.

Some studies have experimentally investigated the impact of adding oxygen impurity to the inlet gas used for the APPJ. For example, Asghar and Galaly [21] added oxygen (0.25%, 0.50%, 1%, and 1.5%) to an argon (Ar) APPJ and found that the oxygen content reduced the plasma temperature as well as the length and intensity of the emission spectra at the nozzle outlet and in the downstream, while oxygen-related species (e.g., O, OH, and NO) increased. Similarly, Komin and Pelipasov [22] mixed 0.1–1.2% O_2 in nitrogen (N_2) microwave-induced plasma (MIP) and found that increasing oxygen content in the inlet mixture reduced the temperature, electric density, and N_2, and N_2 ion species and increased

the NO and OH species. Krumpolec et al. [23] utilized ambient air, nitrogen, a hydrogen–nitrogen mixture, and hydrogen as plasma inlet gas, and this research emphasized that the thermal effect of different inlet gas would affect the selective etching performance.

Tochikubo et al. [24] performed He dielectric barrier discharge (DBD) simulations and found that as the oxygen content in the inlet mixture was increased from 7.5% to 15%, and O atoms increased. Cheng [25] performed He DBD simulations and found that as the oxygen content in the inlet mixture was increased from 0.003% to 0.1%, the electronic density of the plasma and the nitrogen second positive system (SPS) excitation decreased. Other researchers studied humid air as an inlet gas impurity [26] and found that it increased OH in the downstream [27–30].

In this study, we simulated a nitrogen DC pulse APPJ with a quartz tube design [6,7] by using an axisymmetric model that takes into account the fluid dynamics, heat transfer, mass diffusion, and species transfer equations. We used the steady-state assumption because we focused on the treated surface downstream. We added different amounts of oxygen impurities to the nitrogen gas source and investigated the heat and species in the downstream above the substrate.

2. Materials and Methods

A nitrogen DC pulse APPJ with a quartz tube design was simulated using COMSOL Multiphysics 5.3a, in which finite element methods were applied, as illustrated in Figure 1, where ADLN is the nozzle of the plasma source, MRSQ is the quartz tube, and FGWV is the working plate. The inlet gas comes from AH, meets the electron and heat sources at BCJI, and spouts out from the nozzle DK. Then, the plasma gas meets the working plate (FV), at which the treated substrate is usually placed, passes the gap (RT) under the quartz tube, and finally flows to the outside air (NabUV). The details of other materials and applied calculations are shown in Table 1.

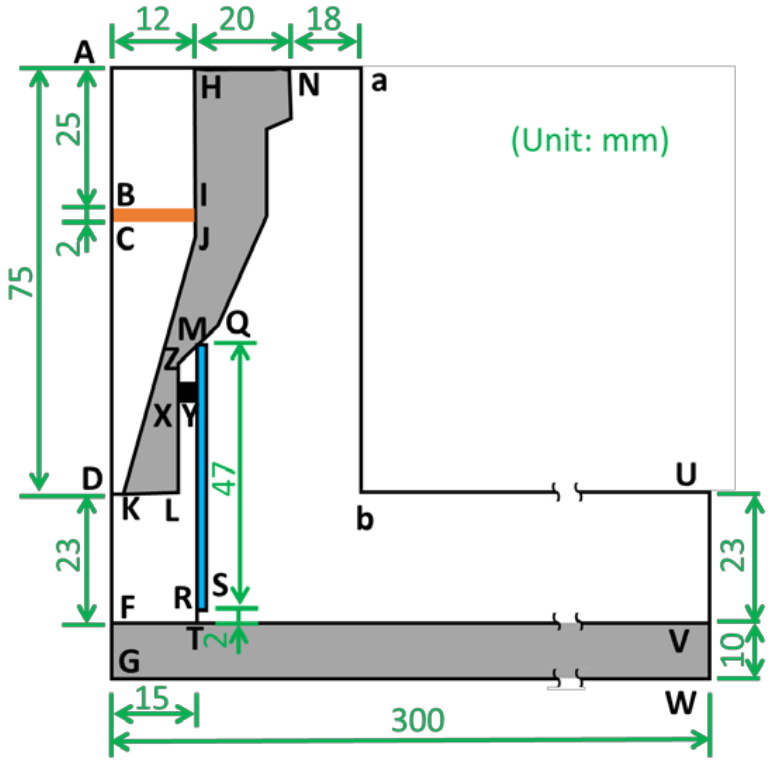


Figure 1. Scheme of the computing model for APPJ.

Table 1. Setting of the computing model domains.

Region	Material	Model/Equation (Parameters)
HKLN	Steel	Heat transfer equation (T)
FGWV	Steel	
MRSQ	Quartz (SiO_2)	
BCJI	N_2 with electron and heat source	Turbulence model (p, $\boldsymbol{u}$, k_{tur}, ω, and G) Species transfer equation (w_i) Diluted species transfer equation (c_i) Heat transfer equation (T)
Others	N_2	

In this study, the turbulence model, heat transfer equation, species transfer equation, and diluted species transfer equation were evaluated. The radius of the nozzle (DK) was 2 mm, the radius of the quartz tube (FT) was 15 mm, the height from nozzle to the substrate (DF) was 23 mm, and the gap from bottom of quartz tube to substrate (RT) was 2 mm. The height and width of the simulated domain were 108 mm and 300 mm, respectively. The mesh consisted of 78,000 elements with 45,000 vertices, where 66,000 triangle elements were for fluid and 120,000 quadratic elements were for solid. Additionally, the meshes of regions with high gradients were locally refined and those of the fluid–solid interfaces had boundary layer refinement. The boundary conditions are described in Table 2 with the inlet nitrogen source of 45 slm. The plasma generation regime (BCJI) was set as a heat source of 1500 W, electron density of 10^{13} cm^{-3}, and electron temperature of 3 eV.

Table 2. Boundary condition settings of the computing model.

Boundary	Turbulent Flow	Species Transfer Equation	Diluted Species Transfer Equation	Heat Transfer Equation
AF	Inflow (45 slm)	Axis symmetry	Concentration (c_i = 0)	Axis symmetry
FG		N/A		
AH		Inflow (w_{N2}/w_{O2})		Inflow (T = 20 °C)
VUbaN	Outflow	Open boundary	Open boundary	Open boundary
GWV and HN		N/A		
HIJKL and FTV and LXYRSQMN	Wall (No slip)	No flux	No flux	Heat flux continuity
MZXY		N/A		Thermal insulation
BI		N/A		Boundary heat source (1500 W)

The Reynolds-averaged Navier–Stokes shear stress transport (RANS SST) turbulence model was applied to the fluid, and the Navier–Stokes equation,

$$\rho(\boldsymbol{u}\cdot\nabla)\boldsymbol{u} = \nabla\cdot\left[-p\boldsymbol{I} + (\mu+\mu_T)\left(\nabla\boldsymbol{u} + (\nabla\boldsymbol{u})^{\boldsymbol{T}}\right) - \frac{2}{3}(\mu+\mu_T)(\nabla\cdot\boldsymbol{u})\boldsymbol{I} - \frac{2}{3}\rho k_{tur}\boldsymbol{I}\right] + \mathbf{F} \quad (1)$$

conservation equation,

$$\nabla\cdot(\rho\boldsymbol{u}) = 0 \quad (2)$$

and turbulence equations

$$\rho(\boldsymbol{u}\cdot\nabla)k_{tur} = \nabla\cdot[(\mu+\mu_T\sigma_k)\nabla k_{tur}] + P_{tur} - \beta_0^*\rho\omega k_{tur} \quad (3)$$

$$\rho(\boldsymbol{u}\cdot\nabla)\omega = \nabla\cdot[(\mu+\mu_T\sigma_\omega)\nabla\omega] + \frac{\gamma}{\mu_T}\rho p - \rho\beta_0\omega^2 + 2(1-f_{v1})\frac{\sigma_{\omega 2}\rho}{\omega}\nabla k_{tur}\cdot\nabla\omega \quad (4)$$

$$\nabla G\cdot\nabla G + \sigma_w G(\nabla\cdot\nabla G) = (1+2\sigma_w)G^4 \quad (5)$$

were applied to solve the pressure (p), velocity field ($\boldsymbol{u}$), turbulent kinetic energy (k_{tur}), specific dissipation rate (ω), and reciprocal wall distance (G), where ρ is density, $\boldsymbol{I}$ is unit matrix, **F** is external force, μ is viscosity, μ_T is turbulent viscosity, and P_{tur} is the production term of turbulent kinetic energy. Other parameters could be found or calculated by the interpolation method in the default setting in the software.

The species transfer equations of N_2, O_2, and N_2O are included in the diffusion model of Fick's law, in which the mass and thermal diffusivity of different gas components are considered.

$$-\nabla\cdot\left(\rho D_i^{fK}\nabla w_i+\rho w_i D_i^{fK}\frac{\nabla M_n}{M_n}-\rho w_i\sum_k\frac{M_i}{M_n}D_k^f\nabla x_k+D_i^T\frac{\nabla T}{T}\right)+\rho(\boldsymbol{u}\cdot\nabla)w_i=R_i \quad (6)$$

where T is temperature, D_i^T is thermal diffusion coefficient, x_k is male fraction, M_i is molar mass, M_n is equivalent molar mass, and R_i denotes the reactions which can be found in Table 3. D_i^{fK} is the equivalent diffusion coefficient and can be calculated from the diffusion coefficient (D_i^f) and the Knudsen diffusion coefficient (D_i^K).

$$D_i^{fK}=\left(\frac{1}{D_i^f}+\frac{1}{D_i^K}\right)^{-1} \quad (7)$$

Therefore, the mixture density of air can be calculated using the ideal gas law depending on the molar mass and mass fraction of N_2, O_2, and N_2O.

$$\rho=\frac{pM_n}{R_gT} \quad (8)$$

Table 3. Reaction rates considered in this computing model.

k	Reaction	Reaction Rate *	Reference
k1	e+N_2→2N+e	$1.249\times10^{-10}\times(11608\times\mathrm{Te})^{0.49}\times\mathrm{e}^{-1.6\times10^5/11608\times\mathrm{Te}}$	[31,32]
k2	e+N_2→N_2(A)+e	$1.23\times10^{-6}\times(11608\times\mathrm{Te})^{-0.47}\times\mathrm{e}^{-1.01\times10^5/11608\times\mathrm{Te}}$	[31,32]
k3	e+N_2→N_2(B)+e	$4.06\times10^{-5}\times(11608\times\mathrm{Te})^{-0.74}\times\mathrm{e}^{-1.17\times10^5/11608\times\mathrm{Te}}$	[31,32]
k4	e+N_2→N_2(C)+e	$8.3\times10^{-11}\times(1.5\times\mathrm{Te})^2\times\mathrm{e}^{-3.43/\mathrm{Te}}$	[31,32]
k5	e+N_2→N_2(a)+e	$1.85\times10^{-11}\times(1.5\times\mathrm{Te})^{1.5747}\times\mathrm{e}^{-2.3658/\mathrm{Te}}$	[31,32]
k6	N_2+N→N_2(A)+N	$1.2\times10^{-12}\times\mathrm{Te}^{-1.5}\times\mathrm{e}^{-6.2/\mathrm{Te}}$	[33]
k7	N+N+M→N_2+M, M=N_2, 100–600 K	$8.3\times10^{-34}\times\mathrm{e}^{500/\mathrm{T}}$	[34]
k8	N+N+M→N_2+M, M=N_2, 600–6300 K	1.91×10^{-33}	[34]
k9	N+N+M→N_2+M, M=O_2, NO, 290–400 K	$1.8\times10^{-33}\times\mathrm{e}^{435/\mathrm{T}}$	[34]
k10	N+N+M→N_2+M, M=O, N	$5.4\times10^{-33}\times\mathrm{e}^{435/\mathrm{T}}$	[34]
k11	N_2+M→N+N+M, M=O_2, NO, N_2	$5.4\times10^{-8}\times\left(1-\mathrm{e}^{-3354/\mathrm{T}}\right)\times\mathrm{e}^{-113200/\mathrm{T}}$	[34]
k12	N_2+M→N+N+M, M=O, N	$3.564\times10^{-7}\times\left(1-\mathrm{e}^{-3354/\mathrm{T}}\right)\times\mathrm{e}^{-113200/\mathrm{T}}$	[34]
k13	N_2+N+N→N_2(A)+N_2	$8.27\times10^{-34}\times\mathrm{e}^{500/\mathrm{T}}$	[32]
k14	N_2(A)+N_2→N_2+N_2	4×10^{-17}	[32,33,35]
k15	N_2(A)+N→N_2+N	9.6×10^{-11}	[32,33,35,36]
k16	N_2+N+N→N_2(B)+N_2	1.2×10^{-33}	[35]
k17	N_2(A)+N_2(A)→N_2(B)+N_2	7.0×10^{-11}	[32,33]
k18	N_2(B)→N_2(A)+hv	1.5×10^{5}	[32,33,35,36]
k19	N_2(B)+N_2→N_2(A)+N_2	5×10^{-11}	[32,35,36]
k20	N_2(A)+N_2(A)→N_2(C)+N_2	3×10^{-10}	[32,33,35,37]
k21	N_2(C)→N_2(B)+hv	3×10^{7}	[32,33,35,36]
k22	N_2(C)+N_2→N_2(a)+N_2	10^{-11}	[36]
k23	N_2(a)+N_2→N_2(B)+N_2	2×10^{-13}	[32,36]

Table 3. *Cont.*

k	Reaction	Reaction Rate *	Reference
k24	$N+O_2 \rightarrow O+NO$, 200 K < T < 300 K	$4.5 \times 10^{-12} \times e^{-3220/T}$	[36]
k25	$N+O_2 \rightarrow O+NO$, T > 300 K	$1.1 \times 10^{-14} \times e^{-3150/T}$	[36]
k26	$N+O+M \rightarrow NO+M$, M=N_2, O_2	$10^{-32} \times (300/T)^{0.5}$	[34]
k27	$N+O+M \rightarrow NO+M$, M=N, O, NO	$1.8 \times 10^{-31} \times (300/T)$	[34]
k28	$N+O \rightarrow NO$	2.39×10^{-13}	[38]
k29	$N+O_3 \rightarrow NO+O_2$	$\leq 2 \times 10^{-16}$	[34,36]
k30	$N+NO \rightarrow O+N_2$	$1.05 \times 10^{-12} \times T^{0.5}$	[32]
k31	$N+NO_2 \rightarrow 2O+N_2$	9.1×10^{-13}	[32]
k32	$N+NO_2 \rightarrow N_2+O_2$	7×10^{-13}	[32]
k33	$N+NO_2 \rightarrow 2NO$	2.3×10^{-12}	[32]
k34	$N+NO_2 \rightarrow N_2O+O$	3×10^{-12}	[32]
k35	$N_2+O_2 \rightarrow O+N_2O$	$2.5 \times 10^{-10} \times e^{-50390/T}$	[34]
k36	$N_2(A)+O \rightarrow N_2+O$	2.5×10^{-11}	[39]
k37	$N_2(A)+O_2 \rightarrow N_2+O+O$	2.54×10^{-12}	[32,36]
k38	$N_2(A)+O_2 \rightarrow N_2O+O$	7.8×10^{-14}	[32,36]
k39	$N_2(A)+NO \rightarrow N_2+NO$	7×10^{-11}	[32,36]
k40	$N_2(A)+N_2O \rightarrow N_2+N+NO$	10^{-11}	[32,36]
k41	$N_2(B)+O_2 \rightarrow N_2+O+O$	3×10^{-10}	[32,36]
k42	$N_2(B)+NO \rightarrow N_2(A)+NO$	2.4×10^{-10}	[32,36]
k43	$N_2(C)+O_2 \rightarrow N_2+O+O$	3×10^{-10}	[36]
k44	$N_2(a)+O_2 \rightarrow N_2+O+O$	2.8×10^{-11}	[32,36]
k45	$N_2(a)+NO \rightarrow N_2+N+O$	3.6×10^{-10}	[32,36]
k46	$O+O+M \rightarrow O_2+M$, M=N_2, 190–500 K	$2.8 \times 10^{-34} \times e^{720/T}$	[34]
k47	$O+O+M \rightarrow O_2+M$, M=N_2, 500–4000 K	$10^{-33} \times (300/T)^{0.41}$	[34]
k48	$O+O+M \rightarrow O_2+M$, M=O_2, 290–4000 K	$4 \times 10^{-33} \times (300/T)^{0.41}$	[34]
k49	$O+O+M \rightarrow O_2+M$, M=N	$3.2 \times 10^{-33} \times (300/T)^{0.41}$	[34]
k50	$O+O+M \rightarrow O_2+M$, M=O	$1.44 \times 10^{-32} \times (300/T)^{0.41}$	[34]
k51	$O+O+M \rightarrow O_2+M$, M=NO	$6.8 \times 10^{-34} \times (300/T)^{0.41}$	[34]
k52	$O+O_2+N_2 \rightarrow O_3+N_2$	$5.8 \times 10^{-34} \times (300/T)^{2.8}$	[34]
k53	$O+O_2+O_2 \rightarrow O_3+O_2$	$7.6 \times 10^{-34} \times (300/T)^{1.9}$	[34]
k54	$O+O_2+N \rightarrow O_3+N$	$3.9 \times 10^{-33} \times (300/T)^{1.9}$	[34]
k55	$O+O_3 \rightarrow O_2+O_2$	$2 \times 10^{-11} \times e^{-2300/T}$	[32,36]
k56	$O+N_2+M \rightarrow N_2O+M$, M=any	$3.9 \times 10^{-35} \times e^{-10400/T}$	[34]
k57	$O+NO \rightarrow NO_2+hv$	4.2×10^{-18}	[32,34]
k58	$O+NO+M \rightarrow NO_2+M$, M=$N_2$	$1.2 \times 10^{-31} \times (300/T)^{1.8}$	[34]
k59	$O+NO+M \rightarrow NO_2+M$, M=$O_2$,NO	$9.36 \times 10^{-32} \times (300/T)^{1.8}$	[34]
k60	$O+NO_2 \rightarrow NO+O_2$	$9.1 \times 10^{-12} \times (T/300)^{0.18}$	[32,34]
k61	$O+NO_3 \rightarrow O_2+NO_2$	10^{-11}	[34,36]
k62	$O+N_2O \rightarrow NO+NO$	$1.5 \times 10^{-10} \times e^{-14090/T}$	[32,34]
k63	$O_2+O_2 \rightarrow O+O_3$	$2 \times 10^{-11} \times e^{-49800/T}$	[34]
k64	$O_2+NO \rightarrow O+NO_2$	$2.8 \times 10^{-12} \times e^{-23400/T}$	[34]
k65	$O_2+NO_2 \rightarrow NO+O_3$	$2.8 \times 10^{-12} \times e^{-25400/T}$	[34]
k66	$O_2+NO_3 \rightarrow NO_2+O_3$	$1.5 \times 10^{-12} \times e^{-15020/T}$	[34]
k67	$O_2+M \rightarrow O+O+M$, M=N_2, N, NO	$6.1 \times 10^{-9} \times \left(1 - e^{-2240/T}\right) \times e^{-59380/T}$	[34]
k68	$O_2+M \rightarrow O+O+M$, M=O_2	$9.67 \times 10^{-8} \times \left(1 - e^{-2240/T}\right) \times e^{-59380/T}$	[34]
k69	$O_2+M \rightarrow O+O+M$, M=O	$1.281 \times 10^{-7} \times \left(1 - e^{-2240/T}\right) \times e^{-59380/T}$	[34]
k70	$O_3+NO \rightarrow O_2+NO_2$	$4.3 \times 10^{-12} \times e^{-1560/T}$	[32,36]
k71	$O_3+NO_2 \rightarrow O_2+NO_3$	$1.2 \times 10^{-13} \times e^{-2450/T}$	[34,36]
k72	$O_3+M \rightarrow O_2+O+M$, M=$N_2$	$6.6 \times 10^{-10} \times e^{-11600/T}$	[34]
k73	$O_3+M \rightarrow O_2+O+M$, M=$O_2$	$2.508 \times 10^{-10} \times e^{-11600/T}$	[34]
k74	$O_3+M \rightarrow O_2+O+M$, M=O, N	$6.3 \times e^{170/T} \times 6.6 \times 10^{-10} \times e^{-11600/T}$	[34]
k75	$NO+NO \rightarrow O+NO_2$	$3.3 \times 10^{-16} \times (300/T)^{0.5} \times e^{-39200/T}$	[34]
k76	$NO+NO_3 \rightarrow NO_2+NO_2$	1.7×10^{-11}	[34,36]

Table 3. *Cont.*

k	Reaction	Reaction Rate *	Reference
k77	$NO_2+NO_2 \rightarrow 2NO+O_2$	$3.3 \times 10^{-12} \times e^{-13500/T}$	[32,34]
k78	$NO_2+NO_3 \rightarrow NO+NO_2+O_2$	$2.3 \times 10^{-13} \times e^{-1600/T}$	[34,36]
k79	$NO_2+M \rightarrow NO+O+M$, M=$N_2$	$6.8 \times 10^{-6} \times (300/T)^2 \times e^{-36180/T}$	[34]
k80	$NO_2+M \rightarrow NO+O+M$, M=$O_2$	$5.304 \times 10^{-6} \times (300/T)^2 \times e^{-36180/T}$	[34]
k81	$NO_2+M \rightarrow NO+O+M$, M=NO	$5.304 \times 10^{-5} \times (300/T)^2 \times e^{-36180/T}$	[34]
k82	$NO_2+M \rightarrow NO+O+M$, M=$NO_2$	$4.012 \times 10^{-5} \times (300/T)^2 \times e^{-36180/T}$	[34]
k83	$NO_3+NO_3 \rightarrow O_2+NO_2+NO_2$	$5 \times 10^{-12} \times e^{-3000/T}$	[36]
k84	$NO_3+M \rightarrow NO_2+O+M$, M=$N_2$, O_2, NO	$3.1 \times 10^{-5} \times (300/T)^2 \times e^{-25000/T}$	[34]
k85	$NO_3+M \rightarrow NO_2+O+M$, M=N, O	$3.1 \times 10^{-4} \times (300/T)^2 \times e^{-25000/T}$	[34]
k86	$NO_3+M \rightarrow NO+O_2+M$, M=$N_2$, O_2, NO	$6.2 \times 10^{-5} \times (300/T)^2 \times e^{-25000/T}$	[34]
k87	$NO_3+M \rightarrow NO+O_2+M$, M=N, O	$7.44 \times 10^{-4} \times (300/T)^2 \times e^{-25000/T}$	[34]

* Unit for reaction rate k: 1/s for first-order reaction, cm^3/s for second-order reaction, and cm^6/s for third-order reaction.

The species considered in the diluted species transfer equation included N_2(A), N_2(B), N_2(C), N_2(a), N, O, O_3, NO, NO_2, and NO_3.

$$\nabla \cdot \left(-D_i^f \nabla c_i \right) + \boldsymbol{u} \cdot \nabla c_i = R_i \tag{9}$$

Because the concentration (c_i) of these rare species is much lower than that of the surrounding air, the calculation of the diluted species and of N_2, O_2, and N_2O should be separated to avoid a numerical round-off error. This transfer equation is based on the diffusion of these rare species and their reactions (R_i); specifically, 87 reactions were considered, as described in Table 3.

The heat transfer model is valid for both the solid and fluid parts.

$$\rho C_p \boldsymbol{u} \cdot \nabla T + \nabla(-k \nabla T) = \mathrm{Q} \cdot \tag{10}$$

where C_p is heat capacity at constant pressure and k is thermal conductivity. The heat sources (Q) included the heat source in the plasma-creating region (BI) and the reaction heats calculated by Hess's law from the species and diluted species transfer equations.

The linear basis function was applied on the abovementioned equations by default in COMSOL Multiphysics 5.3a.

To overcome the convergence issue arising from the combination of complicated equations, iterative and auxiliary calculations are applied in this model. Figure 2 shows the iteration calculation of the computing sequences, where the turbulence model; heat transfer without reaction heats; and species transfer equations of N_2, O_2, and N_2O are calculated first, and then the diluted species transfer equation and heat source are applied. In addition, auxiliary calculations are used in the diluted species transfer equation, where the reaction rates are multiplied by 0.001, 0.01, 0.1, and 1 to reach the real reaction rates. Consequently, the heat and species do not change dramatically, and the model remains stable. After several iterations, the solution convergence is evaluated.

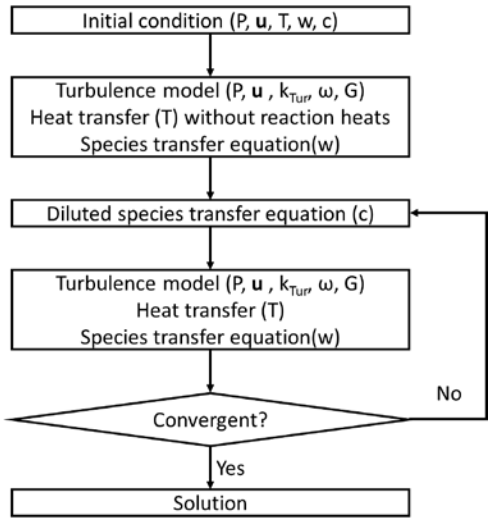


Figure 2. Computing sequence diagram.

3. Results and Discussion

In this study, different amounts of oxygen impurity were added to the nitrogen gas source, with a mix of 10^{-4} O_2, 10^{-3} O_2, and 10^{-2} O_2. Then, the temperature characteristics were discussed through comparisons with experimental data. Further, the individual species distribution on the surface below the quartz tube was determined.

3.1. Temperature Profile

3.1.1. Temperature Profile inside the Quartz Tube

Figure 3 shows the temperature contour of the inlet N_2 with 10^{-3} O_2. The temperature at the nozzle exit was approximately 700 °C, and that at the downstream surface was 500 °C. Because the quartz tube not only prevents excited species from reacting with outside air but also isolates the dissipated heat, the temperature inside the tube was approximately 500 °C.

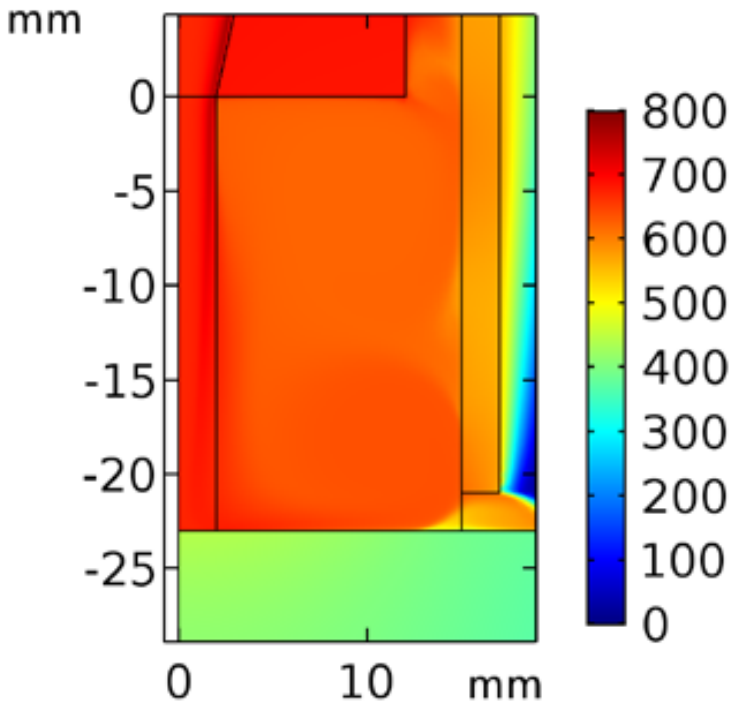


Figure 3. Temperature contour of inlet N_2 with 10^{-3} O_2 in the quartz tube region.

3.1.2. Comparison with Experimental Data

To validate the simulated results, an experiment was performed with a nitrogen DC pulse APPJ with a quartz tube design [6,7] and the same dimensions and inlet gas setting (N_2 with 10^{-3} O_2) as those in the computing model, and the temperature was measured at the plasma equipment. In Figure 4, the inlet gas was supplied from the top of the nozzle exit and excited by electron and heat inside the nozzle. Then, the plasma flowed from the nozzle to the working plate inside the quartz tube, passed through the gap under the quartz tube, and finally mixed with outside air.

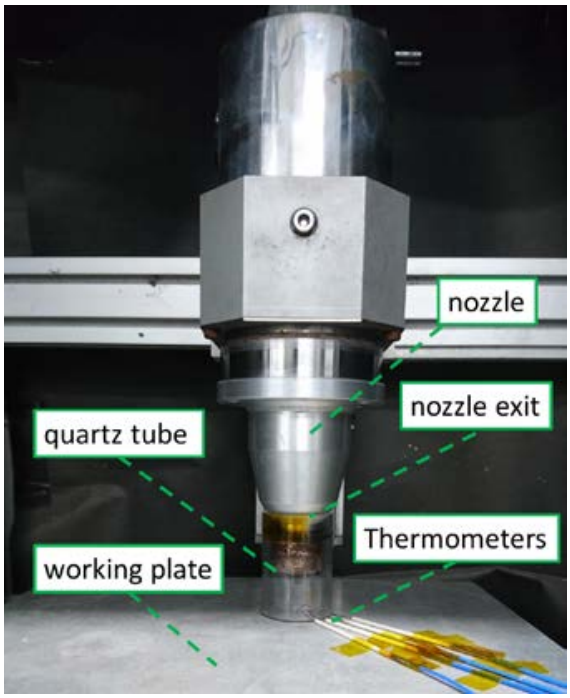


Figure 4. Experimental measurement setup for temperature measurement.

The input voltage was 269 V, and the cycle time was 40 µs with 7 µs on. A K-type thermometer and NI9211 DAQ was used along with Labview data capture software for measuring the temperature. The typical and maximum errors for the K-type thermometer when used with the NI-9211, which account for gain errors, offset errors, differential and integral nonlinearity, quantization errors, noise errors, and isothermal errors, were in the range of 1–1.6 °C and 2–3 °C in the measured temperature range of 0–800 °C. The thermometers were placed on the surface at equal distances, as shown in Figure 4. One set of probes was directly exposed to the air to measure the plasma temperature, and silver glue was applied to another set of probes to obtain the treated surface temperature.

Then, the data on the computing model were divided into two parts: the temperature at FT in Figure 1 on the solid surface and the temperature 0.025 mm above the surface, which mimics the plasma thermal characteristic in air.

The simulated and experimental temperature measurement results were plotted using MATLAB R2022b, as shown in Figure 5. In the experiment, the temperature below the exit (r = 0 mm) was 643 °C in air and 500 °C on the surface, and these temperatures respectively decreased to 538 °C and 417 °C at a radius of 9 mm. However, the simulated temperature profiles were slightly lower than the experimental result below the exit and were slightly overestimated on the surface at a radius of 9 mm. This might be because of the error arising from model domain simplification. For instance, we ignored the heat capacities of some materials and assumed the downstream surface material (FGWV in Figure 1) to be limited to an only 300 mm radius plate even though the radius is approximately 100 cm in reality.

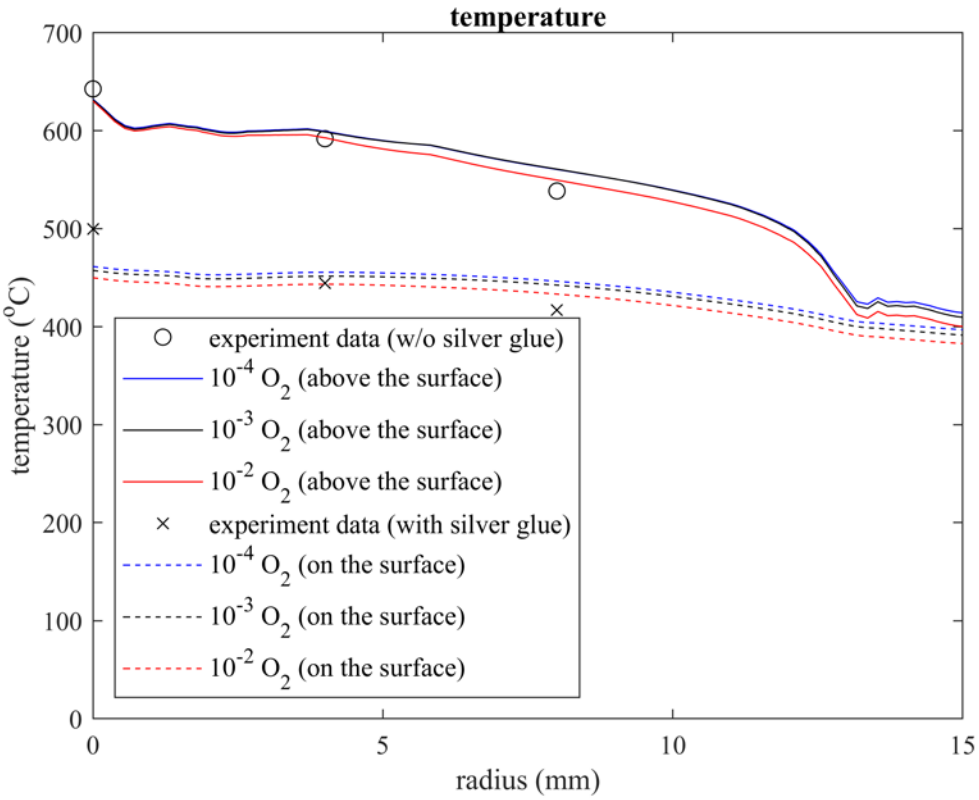


Figure 5. Temperature profile above and on the surface under the quartz tube region, in which the substrate is treated by the plasma.

Both the simulated and experimental temperature profiles agreed with a previous experimental study when different impurities were added to the inlet gas [21,22]. The temperature of 10^{-2} O_2 is slightly lower than that of 10^{-4} O_2; this could be attributed to the endothermic reaction with abundant atomic O, O_2, and O_3 in the quartz tube. Thus, the temperature difference remained within 9 °C, and it could be neglected under the plasma working conditions.

Furthermore, the temperature plot of the simulation data above the surface exhibited a jump at approximately 12.77 mm, where a vortex separation point is also seen in Figure 3. This point could be considered a demarcation between the plasma jet and the incorporation of air from the gap under the quartz tube.

3.2. Species Distribution

To clarify the plasma characteristics, a line probe was set on the surface at FT in Figure 1 to simulate the substrate position that would be treated by the various species.

3.2.1. Distribution of Major Molecules (N_2, O_2)

Figure 6 shows the nitrogen and oxygen distribution on the surface at different radii with the given inlet gas impurities. Below the exit (r = 0 mm), the nitrogen concentration was around 85 mole/m^3, and the oxygen concentrations with inlet gas conditions of 10^{-4} O_2, 10^{-3} O_2, and 10^{-2} O_2 were 0.013 mole/m^3, 0.085 mole/m^3, and 0.76 mole/m^3, respectively. At a distance from the center, the oxygen concentration increased because of the air intruding from the bottom of the quartz tube; at the same time, the nitrogen concentration decreased because nitrogen was oxidized to nitrogen oxide (NO_x).

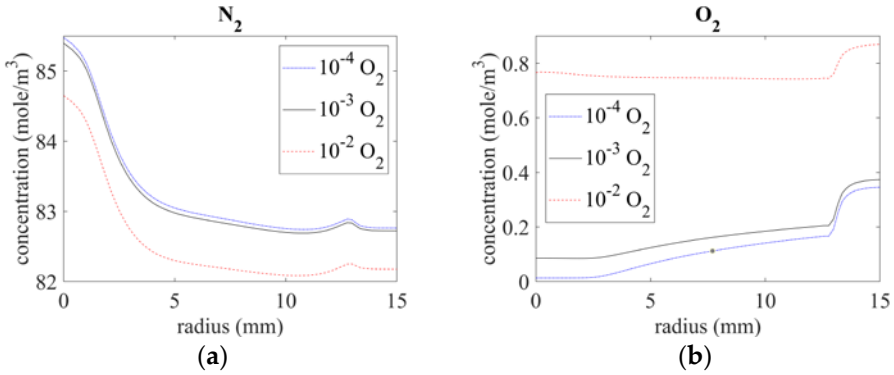


Figure 6. Species distribution of (**a**) N_2 and (**b**) O_2 on the surface.

3.2.2. N-series Species Distribution (N_2(A), N_2(B), N_2(C), N_2(a), N)

The distribution of N-series excited state molecules on the surface is shown in Figure 7. The excited molecules created from the nozzle were clearly dissipated along the downstream. As shown in Figure 7a–e, the concentrations of N_2(A), N_2(B), N_2(C), N_2(a), and N were 10^{-7}, 10^{-12}, 10^{-14}, 10^{-12}, and 10^{-4} mole/m^3 below the exit, and they decreased with increasing distance from the center.

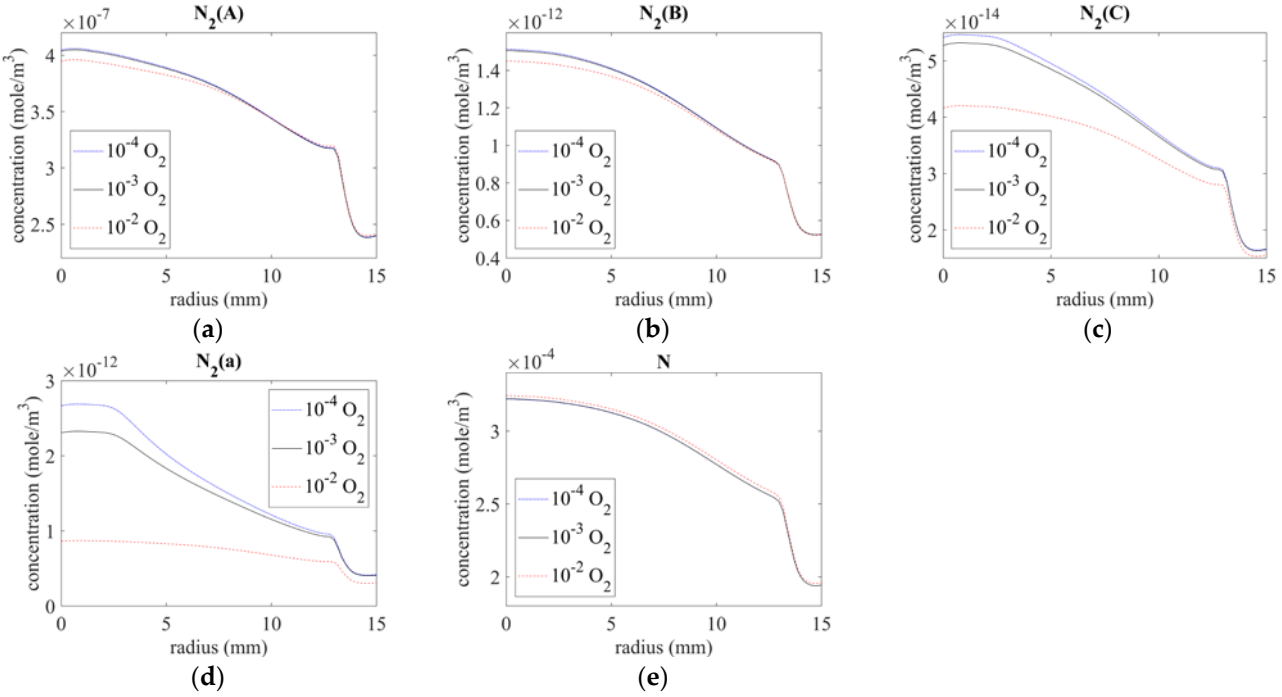


Figure 7. Species distribution on the surface of (**a**) N_2(A), (**b**) N_2(B), (**c**) N_2(C), (**d**) N_2(a), and (**e**) N.

Further, the concentrations of N_2(A), N_2(B), N_2(C), and N_2(a) decreased with increasing oxygen at the inlet, possibly owing to the lower N_2 concentration from the plasma source. By contrast, the concentration of N was only slightly higher for the case of 10^{-2} O_2.

3.2.3. Distribution of O-Series and NO_x Components (O, O_3, N_2O, NO, NO_2, and NO_3)

Figure 8 shows the concentration of the O-series and NO_x components. The inlet gas impurities significantly influence these components. Because oxygen is one of the major reactants with these components, an increase in the amount of oxygen mixed with the inlet gas results in the production of a higher concentration of O-series and NO_x from the nozzle.

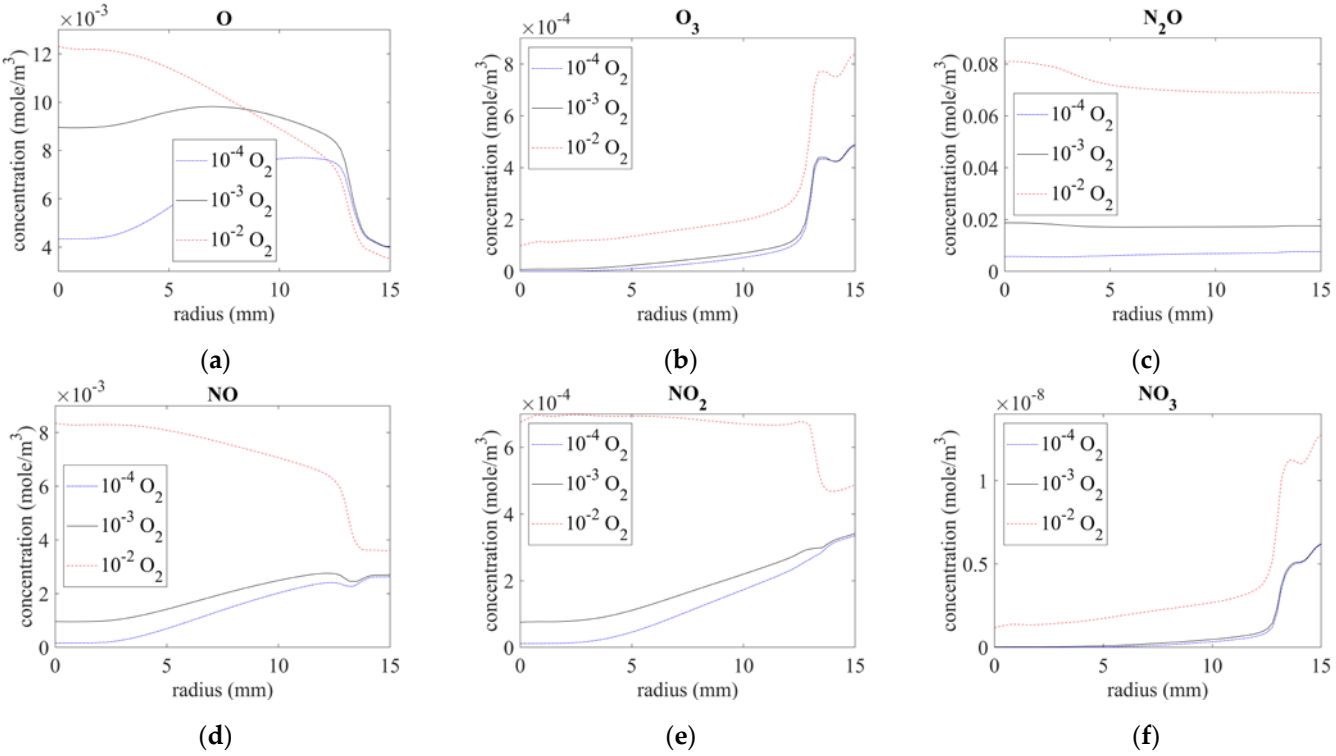


Figure 8. Species distribution on surface of (**a**) O, (**b**) O_3, (**c**) N_2O, (**d**) NO, (**e**) NO_2, and (**f**) NO_3.

Atomic O is a highly active chemical, and it rapidly reaches a stable concentration at atmospheric pressure in combination with intruding surrounding air, as illustrated in Figure 8a. N-series excited components and N_2 react with oxygen from the gap under the quartz tube in the downstream and produce O_3, NO, NO_2, and NO_3. Therefore, O_3 and NO_3 increased by almost ten times below the exit, as shown in Figure 8b,f, respectively, and the same could be seen for NO and NO_2 with impurities of 10^{-4} O_2 and 10^{-3} O_2, as shown in Figure 8d,e, respectively. An impurity of 10^{-2} O_2 seemed to cause saturation for NO and NO_2 such that the concentration decreased along the radius. By contrast, N_2O was relatively stable and exhibited little variation when mixed with downstream air, as shown in Figure 8c.

A jump was seen at approximately 12.77 mm in almost all concentration distribution results in Figures 6–8. This position could be considered a demarcation between the plasma jet and the incorporation of air, as also seen in Figure 3.

4. Discussion & Conclusions

In this study, a simulated model that incorporated the fluid properties, heat transfer, and species transport characteristics was developed. The temperature and species performance on the treated surface were discussed under the addition of different amounts of oxygen impurity. We compared the experimental and simulated temperature profiles and obviously they fit well. Additionally, we found that the temperature slightly dropped when more oxygen was added, which agrees with previous experimental studies [21,22]. With regard to the species concentration, N-related species decreased whereas O- and NO_x-related species increased when more oxygen impurities were added to the inlet nitrogen, and these results agree with previous studies [21,22]. The influence of the inlet gas impurity should be considered when the effect and uniformity of the excited species on the substrate could affect the product performance.

Author Contributions: Conceptualization, J.-Z.C.; methodology, J.-S.T.; software, J.-S.T.; validation, J.-S.T.; formal analysis, J.-S.T.; investigation, J.-S.T. and J.-Z.C.; resources, J.-Z.C.; data curation, J.-S.T.; writing—original draft preparation, J.-S.T.; writing—review and editing, J.-Z.C.; visualization, J.-S.T.; supervision, J.-Z.C.; project administration, J.-Z.C.; funding acquisition, J.-Z.C. All authors have read and agreed to the published version of the manuscript.

Funding: National Science and Technology Council in Taiwan (NSTC 111-2221-E-002-088-MY3 and NSTC 111-3116-F-002-005).

Institutional Review Board Statement: Not applicable.

Informed Consent Statement: Not applicable.

Data Availability Statement: Not applicable.

Acknowledgments: The authors would like to thank Chih-Hung Chen at the Graduate Institute of Applied Mechanics, National Taiwan University, for technical support with the CFD software; Jui-Hsuan Tsai at the Graduate Institute of Applied Mechanics, National Taiwan University, for assistance with the experimental measurement; and Cheng-Che Hsu at the Department of Chemical Engineering, National Taiwan University, for the fruitful discussions on this research. This work is supported by the National Science and Technology Council in Taiwan under grant nos. NSTC 111-2221-E-002-088-MY3 and NSTC 111-3116-F-002-005.

Conflicts of Interest: The authors declare no conflict of interest.

References

1. Schutze, A.; Jeong, J.Y.; Babayan, S.E.; Jaeyoung, P.; Selwyn, G.S.; Hicks, R.F. The atmospheric-pressure plasma jet: A review and comparison to other plasma sources. *IEEE Trans. Plasma Sci.* **1998**, *26*, 1685–1694. [CrossRef]
2. Tendero, C.; Tixier, C.; Tristant, P.; Desmaison, J.; Leprince, P. Atmospheric pressure plasmas: A review. *Spectrochim Acta B* **2006**, *61*, 2–30. [CrossRef]
3. Winter, J.; Brandenburg, R.; Weltmann, K.D. Atmospheric pressure plasma jets: An overview of devices and new directions. *Plasma Sources Sci. Technol.* **2015**, *24*, 064001. [CrossRef]
4. Yáñez-Pacios, A.; Martín-Martínez, J. Comparative Adhesion, Ageing Resistance, and Surface Properties of Wood Plastic Composite Treated with Low Pressure Plasma and Atmospheric Pressure Plasma Jet. *Polymers* **2018**, *10*, 643. [CrossRef] [PubMed]
5. Kong, J.; Du, D.; Song, A.; Zhang, F.; Huang, W. Surface Physical and Chemical Modification of Pure Iron by Using Atmospheric Pressure Plasma Treatment. *Materials* **2020**, *13*, 4775. [CrossRef] [PubMed]
6. Tsai, J.-H.; Cheng, I.C.; Hsu, C.-C.; Chen, J.-Z. DC-pulse atmospheric-pressure plasma jet and dielectric barrier discharge surface treatments on fluorine-doped tin oxide for perovskite solar cell application. *J. Phys. D Appl. Phys.* **2018**, *51*, 025502. [CrossRef]
7. Cheng, P.-Y.; Lu, N.-H.; Lu, Y.-S.; Chen, C.-H.; Lee, Y.-L.; Chen, J.-Z. Surface Modification of FeCoNiCr Medium-Entropy Alloy (MEA) Using Octadecyltrichlorosilane and Atmospheric-Pressure Plasma Jet. *Polymers* **2020**, *12*, 788. [CrossRef]
8. Stryczewska, H.D.; Boiko, O. Applications of Plasma Produced with Electrical Discharges in Gases for Agriculture and Biomedicine. *Appl. Sci.* **2022**, *12*, 4405. [CrossRef]
9. Zhou, Y.; Yan, Y.; Shi, M.; Liu, Y. Effect of an Atmospheric Pressure Plasma Jet on the Structure and Physicochemical Properties of Waxy and Normal Maize Starch. *Polymers* **2018**, *11*, 8. [CrossRef]
10. Cordaro, L.; De Masi, G.; Fassina, A.; Gareri, C.; Pimazzoni, A.; Desideri, D.; Indolfi, C.; Martines, E. The Role of Thermal Effects in Plasma Medical Applications: Biological and Calorimetric Analysis. *Appl. Sci.* **2019**, *9*, 5560. [CrossRef]
11. Domonkos, M.; Tichá, P.; Trejbal, J.; Demo, P. Applications of Cold Atmospheric Pressure Plasma Technology in Medicine, Agriculture and Food Industry. *Appl. Sci.* **2021**, *11*, 4809. [CrossRef]
12. Greb, A.; Niemi, K.; O'Connell, D.; Ennis, G.J.; Macgearailt, N.; Gans, T. Improved fluid simulations of radio-frequency plasmas using energy dependent ion mobilities. *Phys. Plasmas* **2013**, *20*, 053502. [CrossRef]
13. Naidis, G.V.; Babaeva, N.Y. Modeling of streamer dynamics in helium plasma jets driven by modulated voltage pulses. *Phys. Plasmas* **2019**, *26*, 094501. [CrossRef]
14. Tochikubo, F.; Shirai, N.; Uchida, S. Simulation of Atmospheric Pressure Direct Current Glow Discharge along a Miniature Helium Flow in Nitrogen. *Appl. Phys. Express* **2011**, *4*, 056001. [CrossRef]
15. Logothetis, D.K.; Papadopoulos, P.K.; Svarnas, P.; Vafeas, P. Numerical simulation of the interaction between helium jet flow and an atmospheric-pressure "plasma jet". *Comput. Fluids* **2016**, *140*, 11–18. [CrossRef]
16. Passaras, D.N. Simulation of Atmospheric Pressure Plasma Jets with a Global Model. Master's Thesis, National and Kapodistrian University of Athens, Zografou, Greece, 2016.
17. Tsai, J.-H.; Hsu, C.-M.; Hsu, C.-C. Numerical Simulation of Downstream Kinetics of an Atmospheric Pressure Nitrogen Plasma Jet Using Laminar, Modified Laminar, and Turbulent Models. *Plasma Chem. Plasma Process.* **2013**, *33*, 1121–1135. [CrossRef]

18. Lin, K.M.; Hu, M.H.; Hung, C.T.; Wu, J.S.; Hwang, F.N.; Chen, Y.S.; Cheng, G. A parallel hybrid numerical algorithm for simulating gas flow and gas discharge of an atmospheric-pressure plasma jet. *Comput. Phys. Commun.* **2012**, *183*, 2550–2560. [CrossRef]
19. Kuzenov, V.V.; Ryzhkov, S.V.; Starostin, A.V. Pulsed Jets for Dense Plasma Generation in an External Magnetic Field. *Russian Phys. J.* **2020**, *62*, 2041–2045. [CrossRef]
20. Kuzenov, V.V.; Ryzhkov, S.V. Evaluation of the possibility of ignition of a hydrogen-oxygen mixture by erosive flame of the impulse laser. *Laser Phys.* **2019**, *29*, 096001. [CrossRef]
21. Asghar, A.H.; Galaly, A.R. The Effect of Oxygen Admixture with Argon Discharges on the Impact Parameters of Atmospheric Pressure Plasma Jet Characteristics. *Appl. Sci.* **2021**, *11*, 6870. [CrossRef]
22. Komin, O.V.; Pelipasov, O.V. Effect of O_2 in plasma gas on parameters of nitrogen MIP-OES. *J. Anal. Atomic Spectrom.* **2022**, *37*, 1573–1577. [CrossRef]
23. Krumpolec, R.; Jurmanová, J.; Zemánek, M.; Kelar, J.; Kováčik, D.; Černák, M. Selective Plasma Etching of Polymer-Metal Mesh Foil in Large-Area Hydrogen Atmospheric Pressure Plasma. *Appl. Sci.* **2020**, *10*, 7356. [CrossRef]
24. Tochikubo, F.; Uchida, S.; Yasui, H.; Sato, K. Numerical Simulation of NO Oxidation in Dielectric Barrier Discharge with Microdischarge Formation. *Jpn. J. Appl. Phys.* **2009**, *48*, 076507. [CrossRef]
25. Cheng, K.-W. Fluid Modeling of Parallel-Plate Nitrogen-based Dielectric Barrier Discharge Driven by a Realistic Distorted Sinusoidal AC Power Source. Master's Thesis, National Chiao Tung University, Hsinchu, Taiwan, 2012.
26. Sakiyama, Y.; Graves, D.B.; Chang, H.-W.; Shimizu, T.; Morfill, G.E. Plasma chemistry model of surface microdischarge in humid air and dynamics of reactive neutral species. *J. Phys. D Appl. Phys.* **2012**, *45*, 425201. [CrossRef]
27. Nikiforov, A.Y.; Sarani, A.; Leys, C. The influence of water vapor content on electrical and spectral properties of an atmospheric pressure plasma jet. *Plasma Sources Sci. Technol.* **2011**, *20*, 015014. [CrossRef]
28. Lin, K.-M. Development of Parallel Hybrid Simulation of Gas Discharge and Gas Flow and Its Application in the Modeling of Atmospheric-Pressure Helium Dielectric Barrier Discharge Jet Considering Impurities. Master's Thesis, National Chiao Tung University, Hsinchu, Taiwan, 2012.
29. Murakami, T.; Niemi, K.; Gans, T.; O'Connell, D.; Graham, W.G. Chemical kinetics and reactive species in atmospheric pressure helium-oxygen plasmas with humid-air impurities. *Plasma Sources Sci. Technol.* **2013**, *22*, 015003. [CrossRef]
30. Schröter, S.; Gibson, A.R.; Kushner, M.J.; Gans, T.; O'Connell, D. Numerical study of the influence of surface reaction probabilities on reactive species in an rf atmospheric pressure plasma containing humidity. *Plasma Phys. Control. Fusion* **2018**, *60*, 014035. [CrossRef]
31. Itikawa, Y. Cross sections for electron collisions with nitrogen molecules. *J. Phys. Chem. Ref. Data* **2006**, *35*, 31–53. [CrossRef]
32. Tsai, I.H.; Hsu, C.C. Numerical Simulation of Downstream Kinetics of an Atmospheric-Pressure Nitrogen Plasma Jet. *IEEE Trans. Plasma Sci.* **2010**, *38*, 3387–3392. [CrossRef]
33. Moravej, M.; Yang, X.; Barankin, M.; Penelon, J.; Babayan, S.E.; Hicks, R.F. Properties of an atmospheric pressure radio-frequency argon and nitrogen plasma. *Plasma Sources Sci. Technol.* **2006**, *15*, 204–210. [CrossRef]
34. Capitelli, M.; Ferreira, C.M.; Gordiets, B.F.; Osipov, A.I. *Plasma Kinetics in Atmospheric Gases*; Springer: Berlin/Heidelberg, Germany, 2000; p. 300.
35. Babayan, S.E.; Ding, G.; Nowling, G.R.; Yang, X.; Hicks, R.F. Characterization of the active species in the afterglow of a nitrogen and helium atmospheric-pressure plasma. *Plasma Chem. Plasma Process.* **2002**, *22*, 255–269. [CrossRef]
36. Kossyi, I.A.; Kostinsky, A.Y.; Matveyev, A.A.; Silakov, V.P. Kinetic scheme of the non-equilibrium discharge in nitrogen-oxygen mixtures. *Plasma Sources Sci. Technol.* **1992**, *1*, 207–220. [CrossRef]
37. Piper, L.G. State-to-state N2(A 3Σ+u) energy-pooling reactions. I. The formation of N2(C 3Πu) and the Herman infrared system. *J. Chem. Phys.* **1988**, *88*, 231–239. [CrossRef]
38. Uhm, H.S.; Ki, S.H.; Baik, K.Y.; Choi, E.H. Influence of oxygen on generation of reactive chemicals from nitrogen plasma jet. *Sci. Rep.* **2018**, *8*, 9318. [CrossRef] [PubMed]
39. Herron, J.T. Evaluated Chemical Kinetics Data for Reactions of N(2D), N(2P), and N2(A3Σu+) in the Gas Phase. *J. Phys. Chem. Ref. Data* **1999**, *28*, 1453–1483. [CrossRef]

Disclaimer/Publisher's Note: The statements, opinions and data contained in all publications are solely those of the individual author(s) and contributor(s) and not of MDPI and/or the editor(s). MDPI and/or the editor(s) disclaim responsibility for any injury to people or property resulting from any ideas, methods, instructions or products referred to in the content.